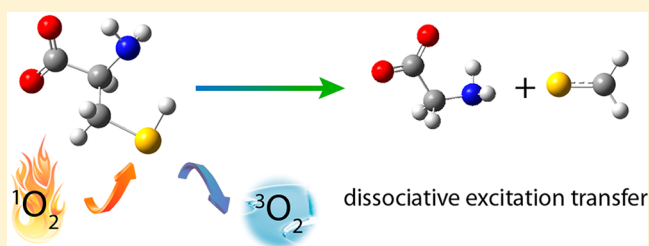


Guided-Ion-Beam Scattering and Direct Dynamics Trajectory Study on the Reaction of Deprotonated Cysteine with Singlet Molecular Oxygen

Yigang Fang, Fangwei Liu, Rifat Emre, and Jianbo Liu*

Department of Chemistry and Biochemistry, Queens College and the Graduate Center of the City University of New York, 65-30 Kissena Boulevard, Queens, New York 11367, United States

ABSTRACT: We present a study on the gas-phase reaction of deprotonated cysteine with the lowest electronically excited state of molecular oxygen $O_2[a^1\Delta_g]$, including the measurement of the effects of collision energy (E_{col}) on reaction cross sections over a center-of-mass E_{col} range from 0.1 to 1.0 eV. Deprotonated cysteine was generated using electrospray ionization, and has a carboxylate anionic structure ($HSCH_2CH(NH_2)CO_2^-$) in the gas phase. Three product ion channels were observed. The dissociation of $HSCH_2CH(NH_2)CO_2^-$ to $NH_2CH_2CO_2^-$ and neutral CH_2S has the largest cross section over the entire E_{col} range. This product channel is driven by the electronic excitation energy of 1O_2 (the so-called dissociative excitation transfer), and is strongly suppressed by E_{col} . Two minor channels correspond to the formation of $HSCH_2C(NH)CO_2^- + H_2O_2$ via abstraction of two hydrogen atoms from $HSCH_2CH(NH_2)CO_2^-$ by 1O_2 , and the formation of $OSCH_2CH(NH_2)CO_2^-$ radical via elimination of $\cdot OH$ from an intermediate complex, respectively. Density functional theory calculations were used to locate various complexes, transition states, and products. Quasi-classical direct dynamics trajectory simulations were carried out at $E_{col} = 0.2$ eV using the B3LYP/4-31G(d) level of theory. Trajectory results were used to guide the construction of a reaction coordinate, discriminate between different mechanisms, and provide additional mechanistic insights. Analysis of trajectories highlights the importance of complex mediation at the early stages of all reactions, and suggests a partially concerted mechanism for H_2O_2 elimination.



I. INTRODUCTION

$O_2[a^1\Delta_g]$, the lowest electronically excited state of molecular oxygen, is a reactive species important in fields ranging from health and medicine to material sciences and atmospheric chemistry.^{1–5} 1O_2 can be generated in biological systems by energy transfer to ground-state 3O_2 from protein-bound or other chromophores on exposure to UV–visible light (i.e., photosensitization⁶), and by a range of enzymatic and nonenzymatic reactions.⁷ Consequently, 1O_2 chemistry plays a significant role in biological aging, diseases, and cell death^{5,7–9} and in photodynamic therapy where 1O_2 is used for cancer treatment.¹⁰

Due to its electron-rich side chain, cysteine (Cys) is one of the most vulnerable residues toward 1O_2 oxidation,^{7,9,11} and is thus rarely present as a free residue at surface-exposed parts of proteins.¹² Most experiments devoted to the elucidation of the Cys oxidation mechanism were carried out in solution,^{13–19} using “photo-oxidation” methods where 1O_2 was generated with UV–visible light in the presence of sensitizers. Oxidation of Cys involves formation of a persulfoxide intermediate (note that persulfoxide is a well-known key intermediate in the reactions of 1O_2 with organic sulfides but less common in 1O_2 + thiol chemistry²⁰), and oxidation products include cystine, oxyacids (RSO_2H and RSO_3H), and other species that remain to be elucidated. Oxidation of Cys to cystine²¹ is particularly important, because controlled oxidation of cysteine residues

and reduction of cystine act as a redox switch to control the structure and function of a number of key proteins.^{9,22} Photo-oxidation of Cys is found to be strongly pH dependent. At high pH (8–11), the reaction is mediated by 1O_2 , while, at low pH (4–6), the reaction is mediated by radicals formed during photosensitization and oxidation of the thiol group to disulfide is suppressed.³

To avoid the complexities arising from photo-oxidation experiments in solution (such as types of sensitizers, light, solvent compositions, pH, and competition between 1O_2 - and radical-mediated reactions) and simply the interpretation of the Cys oxidation mechanism, we have chosen to look at the reaction of Cys with 1O_2 in the gas phase. One advantage of investigating biomolecules in the gas phase is that it allows one to observe single molecules separated from bulk solution environments. In this way, intrinsic reactivity of molecules can be distinguished from solvent effects. We have reported the reaction of protonated Cys ($CysH^+$) with 1O_2 in the gas phase,²³ using electrospray-ionization (ESI)^{24,25} mass spectrometry and guided-ion-beam scattering methods.²⁶ By combining gas-phase experiments and theoretical simulations, we were able to unravel the reaction mechanism and dynamics

Received: January 7, 2013

Revised: February 14, 2013

Published: February 15, 2013

for $\text{CysH}^+ + {}^1\text{O}_2$. In the present study, we extended our investigation to the oxidation of deprotonated cysteine ($[\text{Cys-H}]^-$), attempting to examine the effects of protonation/deprotonation on Cys oxidation. A guided-ion-beam tandem mass spectrometer, coupled with an ESI source, was employed to examine the reaction. To understand and supplement gas-phase experiments, electronic structure calculations were used to construct a reaction coordinate, and direct dynamics trajectory simulations were used to provide additional mechanistic insights.

II. EXPERIMENTAL AND COMPUTATIONAL DETAILS

Experimental Procedures. The experiment was carried out on a homemade guided-ion-beam tandem mass spectrometer that has been previously described in detail.^{23,27–31} Only a brief description is given here, emphasizing key operating parameters.

For this experiment, both mass filters were operated at 2.1 MHz with a m/z range of 1–500. Sample solution was prepared in HPLC grade methanol/water (1:1 vol ratio) containing a mixture of 0.5 mM L-cysteine (121.2 g/mol, 100.1% by titration, EMD Chemicals) and sodium hydroxide (reagent grade, Fisher). The sample solution was sprayed into ambient atmosphere through an electrospray needle at a flow rate of 0.05 mL/h. The electrospray needle was biased at -2540 V relative to ground. Negatively charged droplets formed from electrospray were fed into an ion source chamber via a desolvation capillary which was held at -93 V relative to ground and heated to 155 °C. Liquid droplets underwent desolvation as they passed through the heated capillary, converting to gas-phase negative ions in the source chamber. A skimmer with an orifice of 0.99 mm (Beam Dynamics) is located 3 mm from the capillary end, separating the source chamber and a radio frequency (rf) hexapole ion guide. The skimmer was biased at -25 V relative to ground, and the electrical field imposed between the capillary and the skimmer removed residual solvent molecules attached to ions via collision-induced desolvation. Negative ions emerging from the skimmer were transported into the hexapole ion guide at a pressure of 20 mTorr and underwent collisional cooling and focusing.^{32,33} As characterized by a collision-induced dissociation (CID) experiment,²⁷ the internal energy of primary ions could be described by a Maxwell–Boltzmann distribution at ~ 310 K. Ions subsequently passed into a quadrupole mass filter to remove other ionic species except $[\text{Cys-H}]^-$. At the exit of the mass filter, $[\text{Cys-H}]^-$ ions were collected and focused into an octopole ion guide. The octopole passes through a scattering cell containing neutral reactant gas. The cell pressure was measured by a capacitance manometer (MKS Baratron 690 head and 670 signal conditioner). The ion guide minimizes losses of the reactant and any product ions resulting from scattering. After passing through the scattering cell, unreacted $[\text{Cys-H}]^-$ and product ions drifted to the end of the octopole, mass analyzed by a second quadrupole mass filter, and counted.

The initial kinetic energy distribution of the $[\text{Cys-H}]^-$ ion beam was determined using a retarding potential analysis,³⁴ i.e., measuring the intensity of the $[\text{Cys-H}]^-$ ion beam while scanning the DC bias voltage applied to the octopole. The DC bias voltage also allowed control of the kinetic energy (E_{Lab}) of $[\text{Cys-H}]^-$ ions in the laboratory frame. E_{Lab} is converted into the collision energy (E_{col}) between $[\text{Cys-H}]^-$ and ${}^1\text{O}_2$ in the center-of-mass frame using $E_{\text{col}} = E_{\text{Lab}} \times m_{\text{neutral}} / (m_{\text{ion}} + m_{\text{neutral}})$, where m_{neutral} and m_{ion} are the masses of ${}^1\text{O}_2$ and

$[\text{Cys-H}]^-$, respectively. The $[\text{Cys-H}]^-$ ion beam intensity was 1×10^6 ion/s and constant within 10%. The initial kinetic energy of the ion beam was 0.3 eV, and the energy spread was ~ 0.3 eV which corresponds to an energy spread of ~ 0.1 eV in the center-of-mass frame for the collisions of $[\text{Cys-H}]^-$ with ${}^1\text{O}_2$. Reaction cross sections as a function of E_{col} were calculated from the ratio of product and reactant ion intensities under single ion–molecule collision conditions, calibrated ${}^1\text{O}_2$ pressure, and the effective length of the scattering cell.³⁵

$\text{O}_2(a^1\Delta_g)$ was generated by microwave discharge of O_2/Ar .^{36,37} The presence of Ar improved discharge stability and did not affect the measurements of ${}^1\text{O}_2$ reactions, because Ar is unreactive with $[\text{Cys-H}]^-$ except for CID which could be measured independently. As described before,²⁷ a 1:1 mixture of O_2/Ar continuously flowed through a discharge tube surrounded by an Evenson resonant cavity.³⁸ The cavity was excited by a 2450 MHz microwave generator (Ophos MPG-4), with the microwave power fed into the cavity no more than 18 W and the power reflected from the cavity less than 5 W. The variations of forward and reflected microwave power were controlled to be within 10%, and the *specific energy deposition per molecule* (calculated from the forward and reflected power and the gas density) was determined to be 14 eV. The latter value was used to estimate the ${}^1\text{O}_2$ yield ($\sim 5\%$) in the discharge.³⁷ The discharge tube was cooled to below 55 °C by air blown into the Evenson cavity. The exit end of the discharge tube was coated by mercuric oxide to remove O atoms generated from discharge. The discharge was about 40 cm from the scattering cell entrance, and the light from the discharge was trapped by a Wood's horn to avoid photolysis of ions or production of background ions by photodesorption from the ion guide surface.

To provide reasonable intensities of product ions, we maintained the pressure of O_2/Ar in the scattering cell at 0.33 mTorr. The collision cross section ($\sigma_{\text{collision}}$) for $[\text{Cys-H}]^- + \text{O}_2$, taken as the greater of the ion-induced dipole capture cross section (σ_{capture})³⁹ and the hard-sphere cross section ($\sigma_{\text{hard-sphere}}$, calculated from the orientation-averaged contact radii of $[\text{Cys-H}]^-$ and O_2), is $31\text{--}67$ Å² in the E_{col} range 0.1–1.0 eV. Accordingly, the probability of $[\text{Cys-H}]^-$ undergoing a single collision within the scattering cell is $<17\%$, and that of double collisions is $<4\%$. The majority of $[\text{Cys-H}]^-$ ions passed through the scattering cell without any interaction with O_2 or Ar, hence keeping multiple ion–molecule collisions to an insignificant level.

As a check on reproducibility, the entire experiment was repeated several times and each time we cycled through different E_{col} . The data presented are averages of several independent data sets. The relative error of cross section measurements is $\sim 25\%$. To check the reactivity of $[\text{Cys-H}]^-$ toward ${}^3\text{O}_2$ and Ar, a control experiment was performed under the same conditions except that the microwave discharge was turned off. Recently, we have set up a chemical ${}^1\text{O}_2$ generator, which uses the reaction of $\text{H}_2\text{O}_2 + \text{Cl}_2 + 2\text{KOH} \rightarrow \text{O}_2(a^1\Delta_g)/\text{O}_2(X^3\Sigma_g^-) + 2\text{KCl} + 2\text{H}_2\text{O}$ to generate ${}^1\text{O}_2$ without O and O_3 contaminants.^{23,30,31} We repeated the experiment relying on this chemical ${}^1\text{O}_2$ generator, and the ${}^1\text{O}_2$ concentration was determined by the emission of $\text{O}_2(a^1\Delta_g \rightarrow X^3\Sigma_g^-, \nu = 0-0)$ at 1270 nm⁴⁰ using a cooled InGaAs photodetector.³⁰ A reasonably good agreement was achieved between experiments using microwave discharge and chemical ${}^1\text{O}_2$ generation schemes, respectively.

Computational Methods. To aid in reaction coordinate interpretation, density functional theory (DFT) electronic structure calculations were performed at the B3LYP level of theory with various basis sets including 6-31+G(d), 6-311++G(d,p), and aug-cc-pV5Z, using Gaussian 09.⁴¹ All geometries were optimized by calculating force constants at every step. Vibrational frequencies and zero-point energies (ZPE) were scaled by a factor of 0.955 and 0.981,⁴² respectively. All the transition states (TSs) found were verified as first-order saddle points by frequency calculations, and the vibrational mode with imaginary frequency corresponds to the reaction pathway. Relaxed potential energy surface scans were performed to look for possible barriers during reactant approach and product separation.

Quasi-classical, direct dynamics trajectory simulations were conducted to identify important steps in the reaction coordinate for $[\text{Cys-H}]^- + {}^1\text{O}_2$. The chemical dynamics program VENUS99 of Hase et al.⁴³ was used to set up trajectory initial conditions, and the Hessian-based method of Bakken et al.⁴⁴ implemented in Gaussian was used to propagate each trajectory, with Hessians recalculated every five steps. Because millions of gradients and Hessian evaluations were required, the level of theory used for trajectories was necessarily modest. On the basis of computational speed and the overall level of agreement with experimental and high level benchmark results, we chose the level of B3LYP/4-31G(d) for calculating trajectories. Trajectory integrations were performed with a step size of $0.25 \text{ amu}^{1/2} \text{ b}$ (corresponding to a step size of $\sim 0.5 \text{ fs}$ in trajectory time), which conserved total energy to better than 10^{-4} Hartree. The SCF = XQC option was adopted during trajectory integration so that a quadratically convergent Hartree-Fock (QC-SCF) method^{41,45} was used in case the usual, but much faster, first-order SCF method failed to converge within the allotted number of cycles.

The purpose of our trajectory simulations was to probe the gross features of the collisions between $[\text{Cys-H}]^-$ and ${}^1\text{O}_2$. Particularly, simulations were used to help discover the reaction mechanism, and locate key transition states for reactions when standard TS-searching methods failed. Thus, all 100 trajectories were calculated at an impact parameter b of 0.1 \AA , rather than sampling the b distribution. E_{col} was set at 0.2 eV for simulations. The initial conditions of the reactants were chosen to mimic our experimental conditions. Because $[\text{Cys-H}]^-$ ions were thermalized in the experiment, their initial vibrational and rotational energies in trajectories were sampled from Boltzmann distributions at 300 K . Similarly, ${}^1\text{O}_2$ was close to room temperature in the experiment, so 300 K was used for both rotational and vibrational temperature for ${}^1\text{O}_2$ in simulations. The quasi-classical initial vibrational state was simulated by giving each reactant atom displacement from equilibrium and momentum appropriate to the initial rovibrational state, with random phases for different modes. Both $[\text{Cys-H}]^-$ and ${}^1\text{O}_2$ have ZPE in all vibrational modes. Randomly oriented $[\text{Cys-H}]^-$ and ${}^1\text{O}_2$ were given relative velocities corresponding to the simulated E_{col} . All trajectories started with an initial center-of-mass reactant separation of 7.0 \AA , and were terminated either when the distance between products exceeded 7.2 \AA , or after 3000 steps. The attractive energy between reactants at the separation of 7.0 \AA is no more than 11 meV , most of which was determined to come from a basis set superposition error (BSSE).⁴⁶ Trajectories were calculated on an Intel core 2 quad (3.0 GHz) and core i7 6-core (3.2 GHz)-based 64 bit Linux computational cluster, and

each trajectory took 150–250 CPU hours. gOpenMol⁴⁷ was used for trajectory visualization. Analysis of individual trajectories and statistical analysis of the trajectory ensemble were done with programs written for this purpose.

III. RESULTS AND DISCUSSION

3.1. Gas-Phase Structures of $[\text{Cys-H}]^-$. One issue for interpretation of $[\text{Cys-H}]^-$ chemistry is that Cys has two deprotonation sites leading to two different anionic structures, i.e., the carboxylate anion $\text{HSCH}_2\text{CH}(\text{NH}_2)\text{CO}_2^-$ due to the deprotonation of the backbone carboxylic acid group and the thiolate anion $^- \text{SCH}_2\text{CH}(\text{NH}_2)\text{CO}_2\text{H}$ due to the deprotonation of the thiol group in the side chain. Both $\text{HSCH}_2\text{CH}(\text{NH}_2)\text{CO}_2^-$ and $^- \text{SCH}_2\text{CH}(\text{NH}_2)\text{CO}_2\text{H}$ have various conformations resulting from their structure flexibility. A grid search method⁴⁶ was used to find local minima in their conformational landscape. Each of the torsional angles of the amino acid was rotated systematically through 360° at 60° increments to generate possible conformations of $\text{HSCH}_2\text{CH}(\text{NH}_2)\text{CO}_2^-$ and $^- \text{SCH}_2\text{CH}(\text{NH}_2)\text{CO}_2\text{H}$, the so-called rotamers. Every conformation so generated was subjected to geometry optimization at B3LYP/6-31+G(d) to derive the associated local minimum conformation. Many of the initial conformations were optimized to the same local minimum conformations. These conformations were then optimized at B3LYP/6-311++G(d, p). Their structures and relative energies with respect to $^- \text{SCH}_2\text{CH}(\text{NH}_2)\text{CO}_2\text{H}_1$, the lowest energy conformation of $[\text{Cys-H}]^-$, are summarized in Figure 1.

The conformations in the top three rows of Figure 1 belong to the $^- \text{SCH}_2\text{CH}(\text{NH}_2)\text{CO}_2\text{H}$ structure, differing by the *cis*-/*trans*-configuration of $-\text{COOH}$, the orientation of the $-\text{COOH}$ group with respect to the $-\text{NH}_2$ group, and that of the thiolate group to the backbone. All conformations are stabilized by intramolecular hydrogen bonds except $^- \text{SCH}_2\text{CH}(\text{NH}_2)\text{CO}_2\text{H}_{11}$ and 13. Particularly, strong hydrogen bonds via proton-sharing between the carboxylic acid and thiolate groups occur in the first three low-lying conformers, with the distance of $\text{CO}_2\text{H}\cdots\text{S}$ being $1.94\text{--}1.98 \text{ \AA}$. Shared proton binding motifs also occur to some extent in the fourth and fifth conformers, between the carboxylic acid and amino groups with a distance of $1.80\text{--}1.84 \text{ \AA}$ from the N atom to the H atom of $-\text{COOH}$. The energies of the first five $^- \text{SCH}_2\text{CH}(\text{NH}_2)\text{CO}_2\text{H}$ conformers differ by a maximum of 0.32 eV , and the remaining conformers lie $0.53\text{--}0.86 \text{ eV}$ higher in energy with respect to $^- \text{SCH}_2\text{CH}(\text{NH}_2)\text{CO}_2\text{H}_1$.

$\text{HSCH}_2\text{CH}(\text{NH}_2)\text{CO}_2^-$ conformers are found to be $0.06\text{--}0.37 \text{ eV}$ higher in energy than the lowest energy thiolate conformer. Each of these conformers features an intramolecular hydrogen bond between one of the H atoms of the N-terminus and the deprotonated C-terminus with a $\text{HNH}\cdots\text{COO}$ distance of $2.02\text{--}2.26 \text{ \AA}$. $\text{HSCH}_2\text{CH}(\text{NH}_2)\text{CO}_2^-_1$ and 7 each has a second hydrogen bond of $\text{H}_2\text{N}\cdots\text{HS}$ with a distance of $2.42\text{--}3.03 \text{ \AA}$, while $\text{HSCH}_2\text{CH}(\text{NH}_2)\text{CO}_2^-_2$, 3, and 4 each has a second hydrogen bond of $\text{COO}\cdots\text{HS}$ with a distance of $1.73\text{--}2.26 \text{ \AA}$. The stable conformations we found for the thiolate and carboxylate structures are consistent with previous reports.^{48–51}

The pK_a of the carboxylic acid group (2.0) is 6.2 units smaller than that of the thiol group (8.2) in Cys,⁵² indicating that $[\text{Cys-H}]^-$ should be a carboxylate but not a thiolate in solution. However, disputes arise regarding the structures of $[\text{Cys-H}]^-$ in the gas phase. Our DFT calculation results at B3LYP/6-311++G(d,p), as well as other calculations performed at the B3LYP/6-311++G(d,p)//B3LYP/6-31+G(d),⁵⁰ B3LYP/

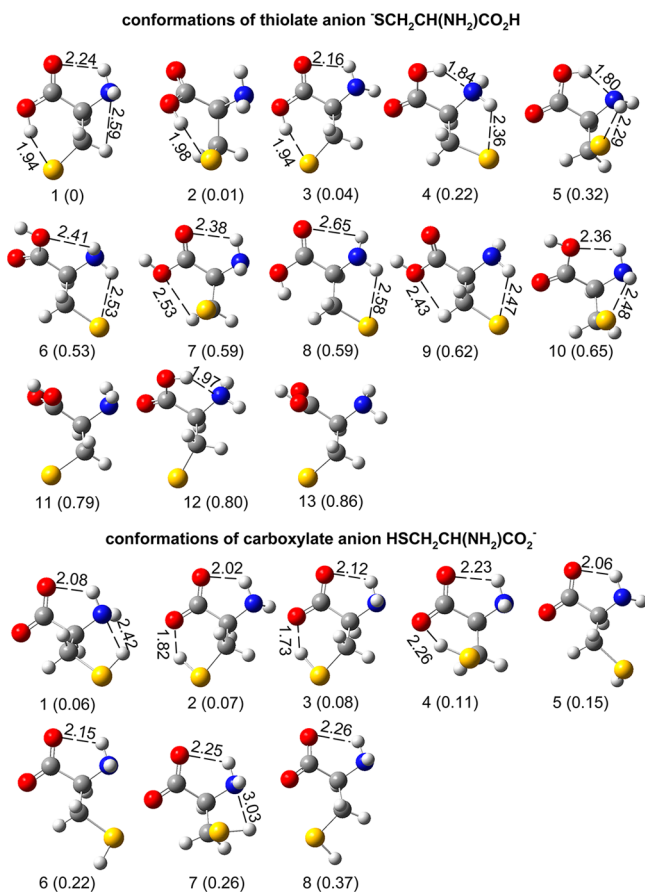


Figure 1. Conformations of $[\text{Cys-H}]^-$ calculated at B3LYP/6-311++G(d,p), including thiolate and carboxylate anionic structures. Their relative energies at 0 K (eV, including ZPE) are indicated below each structure.

aug-cc-pVDZ, and G3B3 levels of theory,⁵¹ reveal that the thiol group of Cys is slightly more acidic than the carboxylic acid group, albeit by a very small margin. Experimentally, Woo et al. claimed that ESI of Cys in 3:1 (v:v) methanol/water solution produced a thiolate in the gas phase according to photoelectron spectroscopy measurements.⁴⁹ Tian et al. found that the preferred deprotonation site for gaseous Cys is the thiol side chain rather than the backbone carboxylic acid based on H/D exchange reactions of $[\text{Cys-H}]^-$ with deuterated alcohols in the gas phase.⁵¹

On the other hand, Oomens et al.⁵³ reported the gas-phase infrared multiple photon dissociation (IRMPD) spectrum of $[\text{Cys-H}]^-$ which was generated by ESI of a mixture of Cys and NaOH in methanol/water. In contrast to PES and H/D exchange studies, the conformation-specific IRMPD spectrum identified a carboxylate structure only for gaseous $[\text{Cys-H}]^-$. It therefore seems that the structures of $[\text{Cys-H}]^-$ present in the gas phase depend on experimental conditions,⁵³ given for instance a similar finding was reported for the carboxylate vs phenoxide structures of deprotonated Tyr in the gas phase.^{31,53–55} In our CID experiment of $[\text{Cys-H}]^-$ with Ar and ${}^3\text{O}_2$ (*vide infra*), overwhelmingly dominant product ions are those of m/z 33, corresponding to the formation of HS^- anions. HS^- is a characteristic fragment of the carboxylate structure, as reported in IRMPD.⁵³ This evidence leads us to conclude that our ESI source produced dominantly carboxylate anions for the reaction with ${}^1\text{O}_2$. In the following calculations

and discussion, we used the most stable $\text{HSCH}_2\text{CH}(\text{NH}_2)\text{CO}_2^-$ conformation in Figure 1 as the reactant ion structure. It is certainly possible that interconversion between different rotamers of $\text{HSCH}_2\text{CH}(\text{NH}_2)\text{CO}_2^-$ may occur during collisions. However, it seems less likely that different rotamers would significantly alter the reaction coordinate, as confirmed by the trajectory simulations of $\text{HSCH}_2\text{CH}(\text{NH}_2)\text{CO}_2^- + {}^1\text{O}_2$ (*vide infra*), $\text{CysH}^+ + {}^1\text{O}_2$,²³ $\text{TyrH}^+ + {}^1\text{O}_2$,²⁷ $[\text{Tyr-H}]^- + {}^1\text{O}_2$,³¹ and $\text{MetH}^+ + {}^1\text{O}_2$.³⁰

3.2. Reaction Cross Sections of $\text{HSCH}_2\text{CH}(\text{NH}_2)\text{CO}_2^- + {}^1\text{O}_2$. For the reaction of $\text{HSCH}_2\text{CH}(\text{NH}_2)\text{CO}_2^- (m/z 120) + {}^1\text{O}_2$, product ions were observed at m/z 74, 118, and 135 over the collision energy range of 0.1–1.0 eV. At higher collision energies, product ions were also observed at m/z 33, 76, 87, and 102, of which m/z 33 is largely dominant. The latter four product ions correspond to the formation of HS^- ,⁵³ and elimination of CO_2 ,⁵⁶ HS , and H_2O ,⁵⁷ respectively, from CID of $\text{HSCH}_2\text{CH}(\text{NH}_2)\text{CO}_2^-$. They were also observed upon collisions of $\text{HSCH}_2\text{CH}(\text{NH}_2)\text{CO}_2^-$ with ${}^3\text{O}_2$ and Ar, and therefore could be excluded from ${}^1\text{O}_2$ -specific reactions. Product ions of m/z 74, 118, and 135, on the other hand, were not observed with ${}^3\text{O}_2$ and Ar, and cannot be attributed to CID products.

Product cross sections of m/z 74 and 118 are shown in Figure 2, as a function of the center-of-mass E_{col} . Note that the

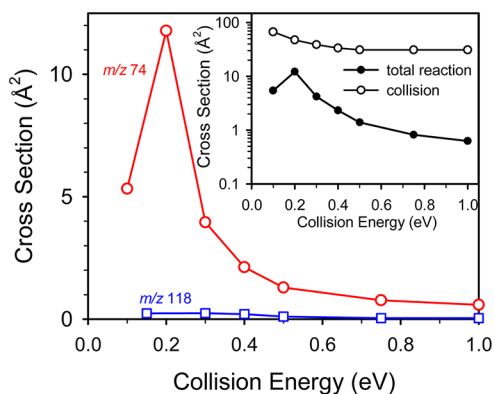


Figure 2. Product cross sections for the reaction of $\text{HSCH}_2\text{CH}(\text{NH}_2)\text{CO}_2^-$ with ${}^1\text{O}_2$, as a function of center-of-mass collision energy. The estimated collision cross section and the total reaction cross section are shown in the inset.

cross section for product ions of m/z 135 is too small to allow for a meaningful measurement of its E_{col} dependence. The structures of these product ions are shown in Figure 3, and will be discussed in the next section. Also shown in the inset of Figure 2 are the experimental total reaction cross section (σ_{total} = sum of individual cross sections) and the estimated collision cross section $\sigma_{\text{collision}}$. We state that the uncertainty in absolute cross section measurements, mostly arising from the uncertainty in the ${}^1\text{O}_2$ concentration, could be large. This source of uncertainty, however, does not affect relative cross sections, i.e., the E_{col} dependence of cross sections. In our ion–molecule scattering experiments, an uncertainty of 25% was quoted for relative cross sections.^{23,27,30,31} Both product channels have significant cross sections only at the lowest energies, and are strongly inhibited by E_{col} . The overall reaction efficiency, estimated as $\sigma_{\text{total}}/\sigma_{\text{collision}}$, is $\sim 25\%$ at low collision energies, dropping to 7% at $E_{\text{col}} = 0.4$ eV and 4% at $E_{\text{col}} = 0.5$ eV, and becoming negligible at $E_{\text{col}} > 0.75$ eV. On the other

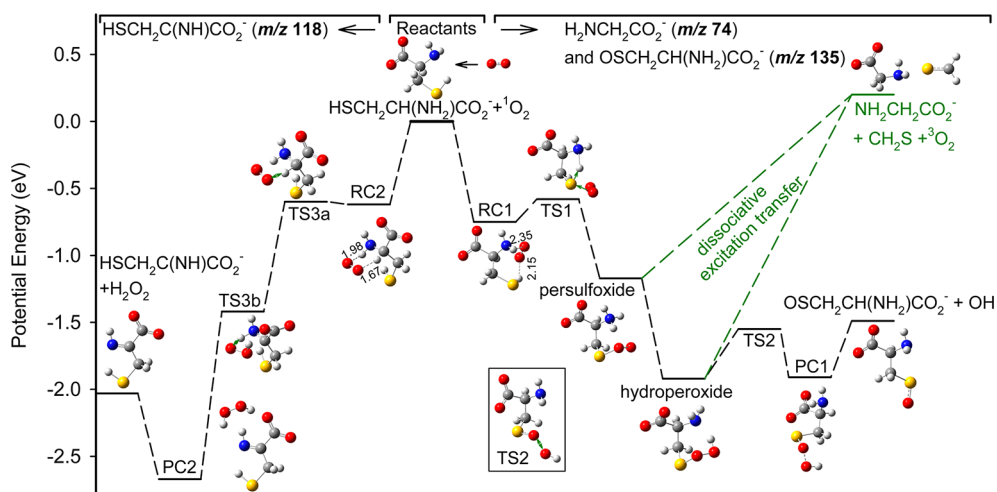
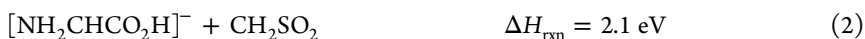


Figure 3. Schematic reaction coordinate for $\text{HSCH}_2\text{CH}(\text{NH}_2)\text{CO}_2^- + {}^1\text{O}_2$. Energies of complexes, TSs, and products, relative to reactants, are derived from a combination of B3LYP/6-31+G(d) and B3LYP/aug-cc-pVSZ results, including ZPE. The bond distances are shown in angstroms. For TSs, vibrational modes corresponding to the imaginary frequencies are indicated by displacement vectors.

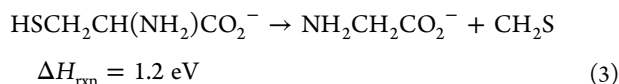
hand, the collision energy dependence of reaction cross sections indicates that both reactions could proceed without significant energy barriers in excess of reactants.

Note that the electron detachment energy for $\text{HSCH}_2\text{CH}(\text{NH}_2)\text{CO}_2^-$ is calculated to be 2.64 eV at B3LYP/6-31+G(d), which is beyond the E_{col} range of 0.1–1.0 eV used in our experiment. Consequently, the detachment of the excess electron from $\text{HSCH}_2\text{CH}(\text{NH}_2)\text{CO}_2^-$ could be disregarded during the collision with target gases. In addition, based on the excitation energy (0.98 eV)⁴⁰ and electron affinity (0.45 eV)⁵⁸



However, both reaction pathways could be discounted based on their reaction heat of formation (ΔH_{rxn}) calculated at B3LYP/6-31+G(d).

If m/z of 74 was produced from unimolecular dissociation of $\text{HSCH}_2\text{CH}(\text{NH}_2)\text{CO}_2^-$, the lowest dissociation energy pathway corresponds to



Because the dissociation energy for reaction 3 is critical for the following discussion of reaction mechanism, this ΔH_{rxn} was calculated using a much larger basis set B3LYP/aug-cc-pVSZ. Reaction 3 involves intramolecular transfer of a H atom from the thiol group to C^α , prior to (or concurring with) $\text{C}^\alpha\text{--C}^\beta$ bond cleavage of $\text{HSC}^\beta\text{H}_2\text{C}^\alpha\text{H}(\text{NH}_2)\text{CO}_2^-$. Obviously, reaction 3 could not occur at E_{col} well below the dissociation threshold (instead, the cross section would rise from zero at an appearance energy near the threshold and increase with E_{col}), unless it is prompted by the excitation energy of ${}^1\text{O}_2$.

Viggiano et al. reported several examples in which the electronic excitation energy of ${}^1\text{O}_2$ was utilized for driving endothermic ion–molecule reactions, such as electron transfer reactions between ${}^1\text{O}_2$ and anions O_2^- , SO_2^- , and HO_2^- ,^{59,60} and dissociation of $\text{OH}^-(\text{H}_2\text{O})_{1,2}$ by the excitation energy of ${}^1\text{O}_2$ —the so-called dissociative excitation transfer.⁶¹ Recently,

of ${}^1\text{O}_2$, electron transfer between $\text{HSCH}_2\text{CH}(\text{NH}_2)\text{CO}_2^-$ and ${}^1\text{O}_2$ is endothermic by 1.21 eV, and thus cannot occur in our E_{col} range, either.

3.3. Reaction Mechanism. A. Product Ion of m/z 74. Complex-Mediated Dissociative Excitation Transfer. The product ion channel of m/z 74 has the largest cross section over the entire E_{col} range. There are two possible reaction pathways leading to the dissociation of an intermediate complex to a product ion of m/z 74, as outlined below:

we reported the gas-phase reaction of CysH^+ with ${}^1\text{O}_2$ and proposed a mechanism based on a similar idea.²³ The reaction of $\text{CysH}^+ + {}^1\text{O}_2$ proceeds via $\text{C}^\alpha\text{--C}^\beta$ bond rupture of a hydroperoxide intermediate CysOOH^+ accompanied by intramolecular H atom transfer. All of the ${}^1\text{O}_2$ excitation energy was used to drive the dissociation of CysOOH^+ , yielding $\text{NH}_2\text{CHCO}_2\text{H}^+$, CH_3SH , and ${}^3\text{O}_2$. Note that, to realize excitation energy transfer in these systems, a strong reactant interaction must be warranted to affect the electronic property of ${}^1\text{O}_2$ and hence break the spin conservation propensity rule.

If a similar scenario occurs for $\text{HSCH}_2\text{CH}(\text{NH}_2)\text{CO}_2^- + {}^1\text{O}_2$, the formation of $\text{NH}_2\text{CH}_2\text{CO}_2^-$ would become energetically feasible at low E_{col} . However, a related question arises as to the nature of energy transfer from ${}^1\text{O}_2$. Two mechanisms may be imaged for dissociation of $\text{HSCH}_2\text{CH}(\text{NH}_2)\text{CO}_2^-$ to $\text{NH}_2\text{CH}_2\text{CO}_2^- + \text{CH}_2\text{S}$. The reaction could proceed in a direct sequential mechanism, as invoked in conventional CID. By this, we mean an activating collision where the excitation energy of ${}^1\text{O}_2$ and a fraction of E_{col} are converted to the internal energy (E_{int}) of $\text{HSCH}_2\text{CH}(\text{NH}_2)\text{CO}_2^-$, followed by unimolecular decomposition of excited $\text{HSCH}_2\text{CH}(\text{NH}_2)\text{CO}_2^-$ after ${}^3\text{O}_2$ has recoiled (i.e., Cys-induced physical quenching of ${}^1\text{O}_2$). However, such a direct sequential mechanism could be ruled out for two reasons. First, a direct collision would likely show E_{col} enhancement rather than inhibition for an endoergic dissociative reaction, since kinetic energy to E_{int} conversion is

helpful for overcoming the reaction threshold as we observed in typical CID reactions.^{62,63} Second, on the basis of DFT calculations, the triplet excited state of HSCH₂CH(NH₂)CO₂⁻ would predissociate to [NH₂CHCH₂ + SH + CO₂]⁻, rendering the energy transfer via intersystem crossing of HSCH₂CH(NH₂)CO₂⁻ + ¹O₂ → ³HSCH₂CH(NH₂)CO₂⁻ + ³O₂ impossible.

An alternative reaction mechanism relies on the formation of a complex between HSCH₂CH(NH₂)CO₂⁻ and ¹O₂, and the electronic energy of ¹O₂ converts into whatever form of *E*_{int} needed for dissociating the complex. The dissociation must be concerted; i.e., O₂ must remain in close proximity to HSCH₂CH(NH₂)CO₂⁻ as HSCH₂CH(NH₂)CO₂⁻ dissociates; in the meantime, strong spin-orbital coupling within the complex could “catalyze” access to the triplet channel with no activation energy in excess of the asymptotic energy for the products. A similar concerted mechanism has been reported for spin-forbidden reactions of NO₂⁺ (¹Σ_g⁺) + Xe → NO⁺ (¹Σ_g⁺) + O(³P) + Xe,⁶² and CysH⁺ + ¹O₂ → NH₂CHCO₂H⁺ + CH₃SH + ³O₂.²³ A complex-mediated mechanism is reasonable for a system like HSCH₂CH(NH₂)CO₂⁻ + ¹O₂, since the number of degrees of freedom is large for efficient *E*_{ele} → *E*_{int} transfer.

A complex-mediated mechanism is also consistent with the observed *E*_{col} dependence of reaction cross section. Production of NH₂CH₂CO₂⁻ + CH₂S requires intramolecular H atom transfer—a rearrangement needs to be mediated by a long-lived complex. The efficiency of complex formation decreases with increasing *E*_{col}, which explains the decreasing of reaction cross section at high *E*_{col}.

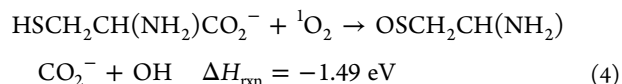
Reaction Coordinate. The potential energy surface (PES) associated with possible low energy reaction pathways for HSCH₂CH(NH₂)CO₂⁻ + ¹O₂ is presented in Figure 3. The reactants are shown near the center at zero energy, and the complex-mediated dissociative excitation transfer between ¹O₂ and HSCH₂CH(NH₂)CO₂⁻ is shown in the right portion of the figure. Energetics are derived from a combination of B3LYP/6-31+G(d) and B3LYP/aug-cc-pV5Z results and the experimental value of ¹O₂ excitation energy. Four weakly bound complexes (RC1 and RC2 and PC1 and PC2) and two covalently bound complexes (a persulfoxide and a hydroperoxide) were identified. The transition states (TSs) connecting the complexes to each other and to the reactants and products are indicated in the figure. The details of the geometries for complexes, TSs, and products are available by request to the corresponding author. Complexes RC1 and RC2 can be characterized as reactant-like complexes, formed by electrostatic interaction and ionic hydrogen bonds. Complex RC1 has the O₂ moiety sandwiched between the thiol and amino groups of HSCH₂CH(NH₂)CO₂⁻, with distances of 2.15 and 2.35 Å for SH...O—O and O—O...HNH, respectively. RC2 is a hydrogen-bonded complex, with both -C^αH and -NH₂ hydrogen bonded to the O₂ moiety with H...O distances of 1.67–1.98 Å. The binding energies of RC1 and RC2 are 0.75 and 0.62 eV, respectively, with respect to the reactants. Because no rearrangement is needed to form reactant-like complexes from the reactants, it is less likely to have significant barriers inhibiting the formation of these two complexes. This was verified by direct dynamics trajectory simulations to be discussed below. Because of a lack of directional covalent bonds between HSCH₂CH(NH₂)CO₂⁻ and O₂ moieties, complexes RC1 and RC2 do not have a well-defined geometry at the energies available in our experiment, and are rather floppy with a large amplitude of intermolecular motion. The

point is that they allow repeated encounters between reactants, increasing reaction probability for collisions not initially in the correct geometry and enhancing the reaction cross section.

RC1 may eventually lead to the formation of a persulfoxide through TS1. Persulfoxide is a covalently bound intermediate, with a binding energy of 1.17 eV relative to the reactants. In the persulfoxide, a H atom is transferred from the thiol group to the amino group. On the basis of a relaxed PES scan, persulfoxide may readily undergo intramolecular H atom transfer from -NH₃ to -SOO without a barrier, converging to a more stable hydroperoxide intermediate. We have also considered a possible C^β-hydrogen abstraction route from the persulfoxide, leading to the formation of a S-hydroperoxysulfonium ylide HOOSC^βHCH(NH₃)CO₂⁻, as observed for ¹O₂ reactions with sulfides by Ishiguro et al.⁶⁴ However, the structure of HOOSC^βHCH(NH₃)CO₂⁻ converged to dissociation products of SCHCH(NH₃)CO₂⁻ (*m/z* 119) + OOH at B3LYP/6-31+G(d). Since product ion of *m/z* 119 was not observed in our experiment, we excluded this route in Figure 3.

We propose that the persulfoxide and/or hydroperoxide may undergo three-body dissociation to NH₂CH₂CO₂⁻, CH₂S, and ³O₂. Intramolecular H atom transfer occurs simultaneously with the dissociation of the persulfoxide or hydroperoxide, transferring a H atom from -NH₃ or -SOOH to the C^α atom. Assuming all of the ¹O₂ excitation energy is contributed to the dissociation of the persulfoxide and/or hydroperoxide, the calculated Δ*H*_{rx} is ~0.2 eV, as indicated by the green line in Figure 3. The calculated Δ*H*_{rx} is consistent with our experimental observation. As shown in Figure 2, the cross section of NH₂CH₂CO₂⁻ generally increases with decreasing *E*_{col} but dips at our lowest *E*_{col}. A dip of this sort is typical for channels that are endoergic but with endoergicity comparable to the *E*_{col} broadening resulting from the distributions of ion beam and target molecule velocities in the experiment. We also note that the reaction endoergicity of 0.2 eV was calculated on the basis of the most stable carboxylate conformer of deprotonated Cys, i.e., HSCH₂CH(NH₂)CO₂⁻₁ in Figure 1. Other conformers such as HSCH₂CH(NH₂)CO₂⁻₂, 3, and 4 with energy within ~0.1 eV of HSCH₂CH(NH₂)CO₂⁻₁ may form in our ESI source and participate in the reaction. Consequently, at the lowest nominal *E*_{col} (i.e., 0.1 eV), a large fraction of collisions have an energy more than the threshold energy, and can react. As a result, the product cross section generally increases with decreasing *E*_{col}, presenting an “exothermic” reaction pattern. Similar *E*_{col} dependence has been reported for an endothermic reaction of H₂CO⁺ + OCS → OCSH⁺ + HCO, with a threshold energy between 0.04 and 0.22 eV.⁶⁵

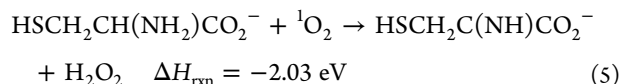
B. Product Ions of *m/z* 135 and 118. Product ion of *m/z* 135 corresponds to the elimination of a OH radical from a reaction intermediate complex. DFT calculations suggest a possible pathway for OH elimination, and its energetics is given as



This reaction follows the same route as that for the formation of NH₂CH₂CO₂⁻, i.e., HSCH₂CH(NH₂)CO₂⁻ + ¹O₂ → RC1 → TS1 → persulfoxide → hydroperoxide, except for the last step at which the hydroperoxide dissociates into a product-like complex PC1 by breaking the peroxide bond. We have located a transition state TS2 between the hydroperoxide and PC1 with

an energy barrier of 0.37 eV above the hydroperoxide (see Figure 3). PC1 is bound by 0.42 eV with respect to the dissociation products, and no reverse barrier separates this product-like complex from $\text{OSCH}_2\text{CH}(\text{NH}_2)\text{CO}_2^- + \text{OH}$. On the basis of the reaction coordinate, $\text{NH}_2\text{CH}_2\text{CO}_2^-$ and $\text{OSCH}_2\text{CH}(\text{NH}_2)\text{CO}_2^-$ are simply two competing channels originating from the decay of the same set of intermediate complexes, i.e., persulfoxide and/or hydroperoxide. However, despite the fact that the product channel of $\text{OSCH}_2\text{CH}(\text{NH}_2)\text{CO}_2^-$ is considerably more energetically favorable than that of $\text{NH}_2\text{CH}_2\text{CO}_2^-$, this channel is insignificant over all collision energies. This discrepancy is not surprising, considering that our calculated PES follows an adiabatic process and is restricted to the singlet state. In reality, two electronic states contribute to the PES; i.e., the system goes from a singlet to a triplet state as the products $\text{NH}_2\text{CH}_2\text{CO}_2^- + \text{CH}_2\text{S} + {}^3\text{O}_2$ separate after dissociative excitation transfer. In addition to chemical reactions, the persulfoxide has the option of decomposing via a physical quenching mode to regenerate the reactant ion and ${}^3\text{O}_2$ as observed in reactions of ${}^1\text{O}_2$ with sulfides.²⁰

Product ion of m/z 118 is another interesting channel, corresponding to the abstraction of two H atoms from $\text{HSCH}_2\text{CH}(\text{NH}_2)\text{CO}_2^-$ by ${}^1\text{O}_2$ to form hydrogen peroxide, and is therefore referred to as the H2T reaction. On the basis of H2T reactions of other amino acids,²⁷ there might exist concerted H2T mechanisms that are difficult to predict using chemical intuitions only. We thus chose to treat the system using quasi-classical, direct dynamics trajectory simulations, where the motion of molecules is followed, allowing the molecules to show us what the preferred reaction pathways are. Trajectory results are discussed in the last section. By following the variations of chemical bonds and potential energies during trajectories, we were able to identify a low energy pathway for H2T which corresponds to



As indicated in the left portion of Figure 3, complex RC2 goes through two consecutive TSs (TS3a and TS3b). At TS3a, which corresponds to a barrier slightly above RC2, the H atom of $-\text{C}^{\alpha}\text{H}$ is transferred to the O_2 moiety. The path from TS3a leads to TS3b, in which the second H atom is transferred from $-\text{NH}_2$ to the other end of the O_2 moiety, leading to a product-like complex PC2 of which two O–H bonds of hydrogen peroxide are fully formed. The calculated reaction coordinate reflects a mainly sequential mechanism, and the rate-limiting step is clearly the transfer of the first H atom as the path from TS3a to TS3b is downhill. However, this mechanism has some character of a concerted reaction, since there is no complex located between two TSs, which has been verified by our trajectories.

3.4. Direct Dynamics Trajectory Simulations. We have completed a total of 100 trajectories at $E_{\text{col}} = 0.2$ eV and $b = 0.1$ Å using the B3LYP/4-31G(d) level of theory. Nearly 10% of collisions either form a persulfoxide and/or hydroperoxide or eliminate H_2O_2 . Remaining trajectories belong to nonreactive collisions, i.e., fly by without forming long-lasting complexes within the simulation time (~ 3 ps).

Figures 4, 5, and 6 demonstrate trajectories representative of nonreactive and reactive collisions of $\text{HSCH}_2\text{CH}(\text{NH}_2)\text{CO}_2^- + {}^1\text{O}_2$, respectively. The plots show the changes of CM distances and potential energy (PE) along the trajectory simulation time.

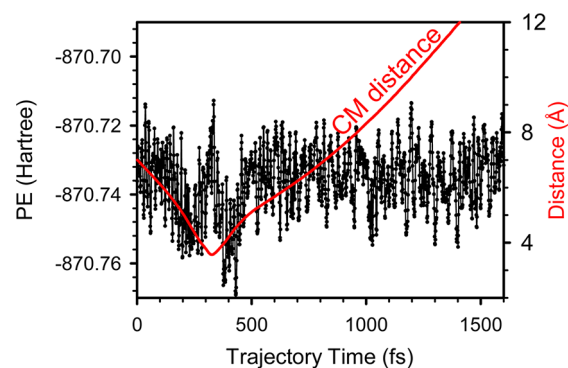


Figure 4. A representative plot of nonreactive trajectories at $E_{\text{col}} = 0.2$ eV, showing the variations of potential energy and center-of-mass distance between $\text{HSCH}_2\text{CH}(\text{NH}_2)\text{CO}_2^-$ and ${}^1\text{O}_2$ moieties during the trajectory.

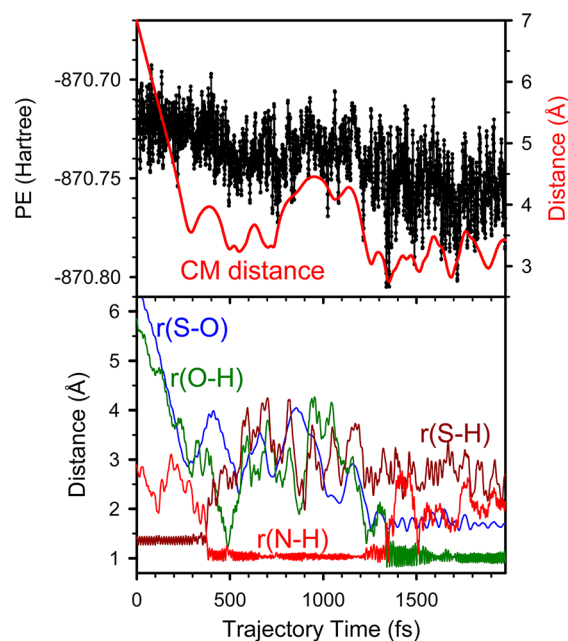


Figure 5. A representative plot of complex-forming trajectories at $E_{\text{col}} = 0.2$ eV: (top) the variations of potential energy and center-of-mass distance between $\text{HSCH}_2\text{CH}(\text{NH}_2)\text{CO}_2^-$ and ${}^1\text{O}_2$ moieties; (bottom) the variations of various bond lengths during the trajectory.

The CM distance is the distance between the centers of mass of the collision partners. Figure 4 shows a direct, nonreactive scattering, with only one turning point in the relative motion of the reactant centers of mass; i.e., there is no sign of mediation by a complex in this collision. The time scale of the collision is somewhat arbitrary, but three numbers are relevant. The time between the start of the trajectory and the onset of strong interaction, which depends on reactant orientation, is around 200 fs. The time for reactant approach within 5 Å of CM distance is around 300 fs. More importantly, the time period during which $\text{HSCH}_2\text{CH}(\text{NH}_2)\text{CO}_2^-$ and ${}^1\text{O}_2$ interact strongly is around 100 fs, as shown by a potential energy spike beginning at $t \approx 300$ fs. During the trajectory, potential energy fluctuates due to the vibrational motions of reactants.

Figure 5 illustrates a complex-forming trajectory, with a similar reactant approach time as that for the nonreactive trajectory shown in Figure 4. The top frame of Figure 5 shows the changes of CM distance and potential energy, and the

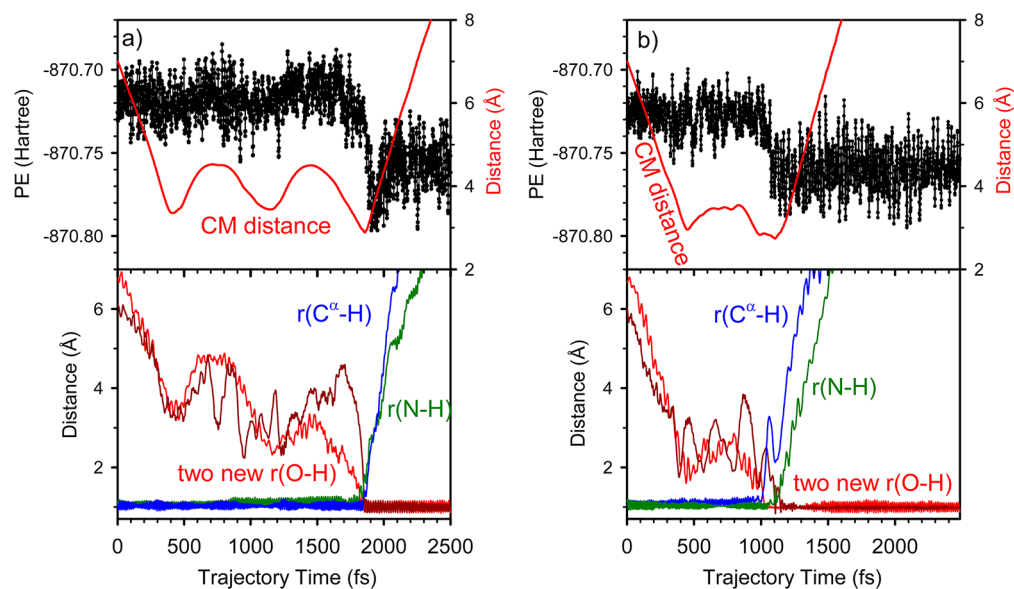


Figure 6. Representative plots of H2T trajectories at $E_{\text{col}} = 0.2$ eV: (a) concerted abstraction of two H atoms; (b) sequential abstraction of two H atoms. (top) The variations of potential energy and center-of-mass distance between reactants or products, and (bottom) the variations of various bond lengths during the trajectory.

bottom frame shows the $r(\text{S}-\text{O})$, $r(\text{O}-\text{H})$, $r(\text{S}-\text{H})$, and $r(\text{N}-\text{H})$ bond lengths forming or breaking in the reaction. The high frequency oscillations of $r(\text{S}-\text{O})$, $r(\text{O}-\text{H})$, $r(\text{S}-\text{H})$, and $r(\text{N}-\text{H})$ reflect the vibrations of the reactants or products. This trajectory initially forms a loosely bound complex, as shown by the decrease of the CM distance to less than 4.5 Å starting at 215 fs. This is followed by the formation of a persulfoxide via transfer of a H atom from the S atom to the N atom, as illustrated by the abrupt increase of $r(\text{S}-\text{H})$ and decrease of $r(\text{N}-\text{H})$ at 350 fs. The large-amplitude, low frequency oscillations of $r(\text{S}-\text{O})$ reflect the interconversion between a weakly bound complex RC and covalently bound persulfoxide. At 1350 fs, the persulfoxide converges to a hydroperoxide as the H atom travels again from the N atom to the peroxide group, as indicated by the simultaneous breaking of $r(\text{N}-\text{H})$ and forming of $r(\text{O}-\text{H})$ at that time point. The trajectory follows the reaction coordinate described in the right portion of Figure 3 until the formation of persulfoxide and hydroperoxide. In agreement with the PES in Figure 3, no obvious potential barrier was observed during the formation of these complexes.

We found that all persulfoxide/hydroperoxide complexes formed in trajectories did not decay back to the reactants before the termination of the trajectories (typically 2–3 ps). This suggests that the lifetime of the complex is at least no less than the trajectory time. For comparison, the classical rotational period of a complex estimated using the average angular momentum is 2.9 ps at $E_{\text{col}} = 0.2$ eV. The fly-by time, taken as the time required for 5 Å motion at the relative speed of reactants, is 0.4 ps at $E_{\text{col}} = 0.2$ eV. The fly-by time gives a measure of how long a direct collision would last at the same collision energy. Clearly, the complex lifetime is significantly longer than the fly-by time, and comparable to the complex rotational period. Note that the quasi-classical trajectory method we used is not applicable to nonadiabatic collisions; i.e., it does not allow transitions from a singlet to a triplet state. Therefore, trajectories cannot reproduce the “spin-forbidden” dissociative excitation transfer or physical quenching of $^1\text{O}_2$. However, trajectories provide information concerning the early time dynamics where the electron spin of the reactants remains

conserved, and more importantly confirming the complex mediation in the reaction.

Finally, two H2T trajectories are illustrated in Figure 6. The $r(\text{C}^\alpha-\text{H})$, $r(\text{N}-\text{H})$, and two $r(\text{O}-\text{H})$ plotted in the figure correspond to the $\text{C}^\alpha-\text{H}$ and $\text{N}-\text{H}$ bonds being broken in $\text{HSCH}_2\text{C}^\alpha\text{H}(\text{NH}_2)\text{CO}_2^-$ and the two new $\text{O}-\text{H}$ bonds being formed in the product H_2O_2 . Figure 6a shows a concerted H2T trajectory, where the $\text{C}^\alpha-\text{H}$ and $\text{N}-\text{H}$ bonds break simultaneously and the two new $\text{O}-\text{H}$ bonds form at the same time. Figure 6b shows a sequential H2T trajectory, where the first H atom is transferred from C^α to O_2 and around 100 fs later the second H is transferred from N to O_2 . These two trajectories together demonstrate the partial concerted nature of the H2T mechanism we have proposed in Figure 3. For both H2T trajectories, the reactants have repeated encounters after their initial collisions and remain close to each other. Actual abstraction of two H atoms occurs around 500 to 1500 fs after initial collisions. This implies that a complex-mediated mechanism is necessary for H2T, as described in the H2T reaction coordinate (see Figure 3).

Note that H2T reactions are only observed in trajectories where the collision geometry allows simultaneous rupture of $\text{C}^\alpha-\text{H}$ and $\text{N}-\text{H}$ bonds in the backbone of Cys by $^1\text{O}_2$. Such a complicated process could occur only in collisions with “ O_2 in close proximity and in parallel to $\text{C}^\alpha\text{H}^*-\text{NH}^*$ ”. This restricted confinement may explain that few collisions could ultimately lead to H2T. On the other hand, the thiol group of cysteine locates at the end of the molecule, leaving more space for O_2 attack. This rationalizes that the trajectory calculated probability for complex-forming reaction is a factor of 5 higher than that of H2T at $b = 0.1$ Å.

IV. CONCLUSIONS

In the present study, guided-ion-beam tandem mass spectrometry was employed to determine the reaction products, cross sections, and collision energy dependence for the reaction of carboxylate anion of deprotonated Cys with $\text{O}_2(a^1\Delta_g)$. DFT

calculations were carried out to identify the reaction coordinate (including reactants, intermediate complexes, transition states, and products) and investigate thermodynamics and energy barriers. Quasi-classical, direct dynamics trajectory simulations were performed for collisions at E_{col} of 0.2 eV and b of 0.1 Å. Trajectories demonstrate the importance of the complex-mediated mechanism for this system, and reveal a number of interesting dynamics features including orientation dependence for various product channels and a partial concerted mechanism for abstraction of two H atoms from Cys by $^1\text{O}_2$. By combining direct dynamics trajectory simulations and reaction coordinate modeling, we are able to ascertain the reaction mechanism for this complicated system. One interesting result is that the electronic excitation energy of $^1\text{O}_2$ can be used to drive the dissociation of deprotonated Cys, yielding the major product ion of $\text{NH}_2\text{CH}_2\text{CO}_2^-$. This dissociative excitation energy transfer is mediated by intermediate complexes.

It is interesting to note that, at the early stage of the reaction, $\text{HSCH}_2\text{CH}(\text{NH}_2)\text{CO}_2^- + ^1\text{O}_2$ shows identical behavior as that of $\text{CysH}^+ + ^1\text{O}_2$.²³ Both protonated and deprotonated Cys form precursor complexes upon collisions with $^1\text{O}_2$, and subsequently interconvert to covalently bound persulfide and hydroperoxide complexes. The dissociation of intermediate complexes by the excitation energy of $^1\text{O}_2$ accounts for the major product channel for both systems, albeit deprotonated Cys has a slightly higher reaction efficiency compared to its protonated analogue. Resemblances also exist between trajectory results calculated at the same E_{col} for these two systems, as both show the importance of complex-mediation for reactive collisions.

AUTHOR INFORMATION

Corresponding Author

*Phone: +1 718 997 3271. Fax: +1 718 997 5531. E-mail: jianbo.liu@qc.cuny.edu.

Notes

The authors declare no competing financial interest.

ACKNOWLEDGMENTS

This work was supported by the National Science Foundation CAREER Award (CHE-0954507), Queens College Research Enhancement Funds, and PSC-CUNY Research Awards. Y.F. acknowledges the CUNY Mina Rees Dissertation Fellowship for 2011–2012.

REFERENCES

- (1) Frimer, A. A. *Singlet O₂, Vol I, Physical-Chemical Aspects*; CRC Press: Boca Raton, FL, 1985.
- (2) Frimer, A. A. *Singlet O₂, Vol II, Reaction Modes and Products, Part I*; CRC Press: Boca Raton, FL, 1985.
- (3) Frimer, A. A. *Singlet O₂, Vol III, Reaction Modes and Products, Part 2*; CRC Press: Boca Raton, FL, 1985.
- (4) Frimer, A. A. *Singlet O₂, Vol IV, Polymers and Biomolecules*; CRC Press: Boca Raton, FL, 1985.
- (5) Ogilby, P. R. Singlet Oxygen: There Is Indeed Something New under the Sun. *Chem. Soc. Rev.* **2010**, *39*, 3181–3209.
- (6) Foote, C. S. Mechanisms of Photosensitized Oxidation. *Science* **1968**, *162*, 963–970.
- (7) Davies, M. J. Singlet Oxygen-Mediated Damage to Proteins and Its Consequences. *Biochem. Biophys. Res. Commun.* **2003**, *305*, 761–770.
- (8) Morgan, P. E.; Dean, R. T.; Davies, M. J. Protective Mechanisms against Peptide and Protein Peroxides Generated by Singlet Oxygen. *Free Radical Biol. Med.* **2004**, *36*, 484–496.
- (9) Davies, M. J. The Oxidative Environment and Protein Damage. *Biochim. Biophys. Acta* **2005**, *1703*, 93–109.
- (10) Palumbo, G. Photodynamic Therapy and Cancer: A Brief Sightseeing Tour. *Expert Opin. Drug Delivery* **2007**, *4*, 131–148.
- (11) Davies, M. J. Reactive Species Formed on Proteins Exposed to Singlet Oxygen. *Photochem. Photobiol. Sci.* **2004**, *3*, 17–25.
- (12) Hedin, E. M. K.; Patkar, S. A.; Vind, J.; Svendsen, A.; Hult, K.; Berglund, P. Selective Reduction and Chemical Modification of Oxidized Lipase Cysteine Mutants. *Can. J. Chem.* **2002**, *80*, 529–539.
- (13) Fishman, P. H.; Kusiak, J. W.; Bailey, J. M. Mutarotase. Photooxidation Reactions and Nature of the Enzyme Catalysis. *Biochemistry* **1973**, *12*, 2540–2544.
- (14) Gennari, G.; Cauzzo, G.; Jori, G. Further Studies on the Crystal-Violet-Sensitized Photooxidation of Cysteine to Cysteic Acid. *Photochem. Photobiol.* **1974**, *20*, 497–500.
- (15) Cannistraro, S.; Jori, G.; Van der Vorst, A. Photosensitization of Amino Acids by Di-Cyan-Hemin: Kinetic and EPR Studies. *Photochem. Photobiol.* **1978**, *27*, 517–521.
- (16) Straight, R. C.; Spikes, J. D. Photosensitized Oxidation of Biomolecules. In *Singlet O₂*; Frimer, A. A., Ed.; CRC Press: Boca Raton, FL, 1985; Vol. IV: Polymers and Biomolecules, pp 91–143.
- (17) Ando, W.; Takata, T. Photooxidation of Sulfur Compounds. In *Singlet O₂*; Frimer, A. A., Ed.; CRC Press: Boca Raton, FL, 1985; Vol. III: Reaction Modes and Products Part 2, pp 1–117.
- (18) Rougee, M.; Bensasson, R. V.; Land, E. J.; Pariente, R. Deactivation of Singlet Molecular Oxygen by Thiols and Related Compounds, Possible Protectors against Skin Photosensitivity. *Photochem. Photobiol.* **1988**, *47*, 485–489.
- (19) Justo, G. Z.; Camargo, F. A.; Haun, M.; Faljoni-Alario, A.; Duran, N. Sensitized Photooxygenation and Peroxidase-Catalyzed Inactivation of Xanthine Oxidase - Evidence of Cysteine Damage by Singlet Oxygen. *Physiol. Chem. Phys. Med. NMR* **2000**, *32*, 145–154.
- (20) Clennan, E. L. Persulfide: Key Intermediate in Reactions of Singlet Oxygen with Sulfides. *Acc. Chem. Res.* **2001**, *34*, 875–884.
- (21) Gracanin, M.; Hawkins, C. L.; Pattison, D. I.; Davies, M. J. Singlet-Oxygen-Mediated Amino Acid and Protein Oxidation: Formation of Tryptophan Peroxides and Decomposition Products. *Free Radical Biol. Med.* **2009**, *47*, 92–102.
- (22) Hogg, P. J. Disulfide Bonds as Switches for Protein Function. *Trends Biochem. Sci.* **2003**, *28*, 210–214.
- (23) Liu, F.; Fang, Y.; Chen, Y.; Liu, J. Dissociative Excitation Energy Transfer in the Reactions of Protonated Cysteine and Tryptophan with Electronically Excited Singlet Molecular Oxygen ($a^1\Delta_g$). *J. Phys. Chem. B* **2011**, *115*, 9898–9909.
- (24) Yamashita, M.; Fenn, J. B. Electrospray Ion Source. Another Variation on the Free-Jet Theme. *J. Phys. Chem.* **1984**, *88*, 4451–4459.
- (25) Fenn, J. B.; Mann, M.; Meng, C. K.; Wong, S. F.; Whitehouse, C. M. Electrospray Ionization for Mass Spectrometry of Large Biomolecules. *Science* **1989**, *246*, 64–71.
- (26) Gerlich, D. Inhomogeneous RF Fields: A Versatile Tool for the Study of Processes with Slow Ions. In *State-Selected and State-to-State Ion-Molecule Reaction Dynamics. Part 1. Experiment*; Ng, C. Y., Baer, M., Eds.; John Wiley & Sons, Inc.: New York, 1992; Vol. 82, pp 1–176.
- (27) Fang, Y.; Liu, J. Reaction of Protonated Tyrosine with Electronically Excited Singlet Molecular Oxygen: An Experimental and Trajectory Study. *J. Phys. Chem. A* **2009**, *113*, 11250–11261.
- (28) Fang, Y.; Bennett, A.; Liu, J. Multiply Charged Gas-Phase NaAOT Reverse Micelles: Formation, Encapsulation and Collision-Induced Dissociation. *Int. J. Mass Spectrom.* **2010**, *293*, 12–22.
- (29) Fang, Y.; Bennett, A.; Liu, J. Selective Transport of Amino Acids into the Gas Phase: Driving Forces for Amino Acid Solubilization in Gas-Phase Reverse Micelles. *Phys. Chem. Chem. Phys.* **2011**, *13*, 1466–1478.
- (30) Fang, Y.; Liu, F.; Bennett, A.; Ara, S.; Liu, J. Experimental and Trajectory Study on Reaction of Protonated Methionine with Electronically Excited Singlet Molecular Oxygen ($a^1\Delta_g$): Reaction Dynamics and Collision Energy Effects. *J. Phys. Chem. B* **2011**, *115*, 2671–2682.

- (31) Liu, F.; Fang, Y.; Chen, Y.; Liu, J. Reactions of Deprotonated Tyrosine and Tryptophan with Electronically Excited Singlet Molecular Oxygen ($a^1\Delta_g$): A Guided-Ion-Beam Scattering, Statistical Modeling, and Trajectory Study. *J. Phys. Chem. B* **2012**, *116*, 6369–6379.
- (32) Moision, R. M.; Armentrout, P. B. An Electrospray Ionization Source for Thermochemical Investigation with the Guided Ion Beam Mass Spectrometer. *J. Am. Soc. Mass Spectrom.* **2007**, *18*, 1124–1134.
- (33) Krutchinsky, A. N.; Chernushevich, I. V.; Spicer, V. L.; Ens, W.; Standing, K. G. Collisional Damping Interface for an Electrospray Ionization Time-of-Flight Mass Spectrometer. *J. Am. Soc. Mass Spectrom.* **1998**, *9*, 569–579.
- (34) Ervin, K. M.; Armentrout, P. B. Translational Energy Dependence of $Ar^+ + XY \rightarrow ArX^+ + Y$ ($XY = H_2, D_2, HD$) from Thermal to 30 eV. *J. Chem. Phys.* **1985**, *83*, 166–189.
- (35) Armentrout, P. B. Fundamental of Ion–Molecule Chemistry. *J. Anal. At. Spectrom.* **2004**, *19*, 571–580.
- (36) Ogrzylo, E. A. Gaseous Singlet Oxygen. In *Singlet Oxygen*; Wasserman, H. H., Murray, R. W., Eds.; Academic Press, Inc.: New York, 1979; pp 35–58.
- (37) Popović, S.; Rašković, M.; Kuo, S. P.; Vušković, L. Reactive Oxygen Emission from Microwave Discharge Plasmas. *J. Phys.: Conf. Ser.* **2007**, *86*, 012013.
- (38) Fehsenfeld, F. C.; Evenson, K. M.; Broida, H. P. Microwave Discharge Cavities Operating at 2450 MHz. *Rev. Sci. Instrum.* **1965**, *36*, 294–298.
- (39) Troe, J. Statistical Adiabatic Channel Model of Ion-Neutral Dipole Capture Rate Constants. *Chem. Phys. Lett.* **1985**, *122*, 425–430.
- (40) Lafferty, W. J.; Solodov, A. M.; Lugez, C. L.; Fraser, G. T. Rotational Line Strengths and Self-Pressure-Broadening Coefficients for the $1.27 \mu\text{m}, a^1\Delta_g-X^3\Sigma_g^-, v = 0-0$ Band of O_2 . *Appl. Opt.* **1998**, *37*, 2264–2270.
- (41) Frisch, M. J.; Trucks, G. W.; Schlegel, H. B.; Scuseria, G. E.; Robb, M. A.; Cheeseman, J. R.; Scalmani, G.; Barone, V.; Mennucci, B.; Petersson, G. A.; et al.; Gaussian 09, rev. B.01; Gaussian, Inc.: Wallingford, CT, 2009.
- (42) Zheng, J.; Alecu, I. M.; Lynch, B. J.; Zhao, Y.; Truhlar, D. G. Database of Frequency Scale Factors for Electronic Model Chemistries, Ver. 2; <http://comp.chem.umn.edu/freqscale/version2.htm>, 2010.
- (43) Hase, W. L.; Bolton, K.; de Sainte Claire, P.; Duchovic, R. J.; Hu, X.; Komornicki, A.; Li, G.; Lim, K.; Lu, D.; Peslherbe, G. H.; et al. *Venus 99: A General Chemical Dynamics Computer Program*; Texas Tech University: Lubbock, TX, 1999.
- (44) Bakken, V.; Millam, J. M.; Schlegel, H. B. Ab Initio Classical Trajectories on the Born-Oppenheimer Surface: Updating Methods for Hessian-Based Integrators. *J. Chem. Phys.* **1999**, *111*, 8773–8777.
- (45) Bacskay, G. B. A Quadratically Convergent Hartree-Fock (QC-SCF) Method. Application to Closed Shell Systems. *Chem. Phys.* **1981**, *61*, 385–404.
- (46) Leach, A. R. *Molecular Modeling: Principles and Applications*; Pearson, Prentice Hall: Harlow, England, 2001.
- (47) Laaksonen, L. *gOpenMol*, 3.0 ed.; Center for Scientific Computing: Espoo, Finland, 2005; available at www.csc.fi/gopenmol/.
- (48) O'Hair, R. A. J.; Bowie, J. H.; Gronert, S. Gas Phase Acidities of the α Amino Acids. *Int. J. Mass Spectrom. Ion Processes* **1992**, *117*, 23–36.
- (49) Woo, H.-K.; Lau, K.-C.; Wang, X.-B.; Wang, L.-S. Observation of Cysteine Thiolate and $^-S\cdots H-O$ Intermolecular Hydrogen Bond. *J. Phys. Chem. A* **2006**, *110*, 12603–12606.
- (50) Jones, C. M.; Bernier, M.; Carson, E.; Colyer, K. E.; Metz, R.; Pawlow, A.; Wischow, E. D.; Webb, I.; Andriole, E. J.; Poutsma, J. C. Gas-Phase Acidities of the 20 Protein Amino Acids. *Int. J. Mass Spectrom.* **2007**, *267*, 54–62.
- (51) Tian, Z.; Pawlow, A.; Poutsma, J. C.; Kass, S. R. Are Carboxyl Groups the Most Acidic Sites in Amino Acids? Gas-Phase Acidity, H/D Exchange Experiments, and Computations on Cysteine and Its Conjugate Base. *J. Am. Chem. Soc.* **2007**, *129*, 5403–5407.
- (52) Vollhardt, P.; Schore, N. *Organic Chemistry*, 6th ed.; W. H. Freeman and Company: New York, 2009.
- (53) Oomens, J.; Steill, J. D.; Redlich, B. Gas-Phase IR Spectroscopy of Deprotonated Amino Acids. *J. Am. Chem. Soc.* **2009**, *131*, 4310–4319.
- (54) Tian, Z.; Kass, S. R. Does Electrospray Ionization Produce Gas-Phase or Liquid-Phase Structures? *J. Am. Chem. Soc.* **2008**, *130*, 10842–10843.
- (55) Tian, Z.; Wang, X.-B.; Wang, L.-S.; Kass, S. R. Are Carboxyl Groups the Most Acidic Sites in Amino Acids? Gas-Phase Acidities, Photoelectron Spectra, and Computations on Tyrosine, *p*-Hydroxybenzoic Acid, and Their Conjugate Bases. *J. Am. Chem. Soc.* **2009**, *131*, 1174–1181.
- (56) Eckersley, M.; Bowie, J. H.; Hayes, R. N. Collision-Induced Dissociations of Deprotonated α -Amino Acids. The Occurrence of Specific Proton Transfers Preceding Fragmentation. *Int. J. Mass Spectrom.* **1989**, *93*, 199–213.
- (57) Kulik, W.; Heerma, W. A Study of the Positive and Negative Ion Fast Atom Bombardment Mass Spectra of α -Amino Acids. *Biomed. Environ. Mass Spectrom.* **1988**, *15*, 419–427.
- (58) Ervin, K. M.; Anusiewicz, I.; Skurski, P.; Simons, J.; Lineberger, W. C. The Only Stable State of O_2^- Is the $X^2\Pi_g$ Ground State and It (Still!) Has an Adiabatic Electron Detachment Energy of 0.45 eV. *J. Phys. Chem. A* **2003**, *107*, 8521–8529.
- (59) Midey, A.; Dotan, I.; Viggiano, A. A. Temperature Dependences for the Reactions of O^- and O_2^- with $O_2(a^1\Delta_g)$ from 200 to 700 K. *J. Phys. Chem. A* **2008**, *112*, 3040–3045.
- (60) Midey, A.; Dotan, I.; Seeley, J. V.; Viggiano, A. A. Reactions of Small Negative Ions with $O_2(a^1\Delta_g)$ and $O_2(X^3\Sigma_g^-)$. *Int. J. Mass Spectrom.* **2009**, *280*, 6–11.
- (61) Viggiano, A. A.; Midey, A.; Eyet, N.; Bierbaum, V. M.; Troe, J. Dissociative Excitation Transfer in the Reaction of $O_2(a^1\Delta_g)$ with $OH^-(H_2O)_{1,2}$ Clusters. *J. Chem. Phys.* **2009**, *131*, 094303.
- (62) Liu, J.; Uselman, B.; Boyle, J.; Anderson, S. L. The Effects of Collision Energy, Vibrational Mode and Vibrational Angular Momentum on Energy Transfer and Dissociation in NO_2^+ -Rare Gas Collisions: An Experimental and Trajectory Study. *J. Chem. Phys.* **2006**, *125*, 133115.
- (63) Liu, J.; van Devener, B.; Anderson, S. L. Collision-Induced Dissociation of Formaldehyde Cations: The Effects of Vibrational Mode, Collision Energy, and Impact Parameter. *J. Chem. Phys.* **2002**, *116*, 5530–5543.
- (64) Ishiguro, K.; Hayashi, M.; Sawaki, Y. Mechanism of Sulfone Formation in the Reaction of Sulfides and Singlet Oxygen: Intermediacy of S-Hydroperoxysulfonium Ylide. *J. Am. Chem. Soc.* **1996**, *118*, 7265–7271.
- (65) Liu, J.; van Devener, B.; Anderson, S. L. The Effects of Vibrational Mode and Collision Energy on the Reaction of Formaldehyde Cation with Carbonyl Sulfide. *J. Chem. Phys.* **2002**, *117*, 8292–8307.